Tribology International 212 (2025) 110967

Contents lists available at ScienceDirect

Tribology International

journal homepage: www.elsevier.com/locate/triboint

Full Length Article

New interpretations of the Elrod–Adams cavitation model

Matti Schultz *, Hannah Orgassa, Michael Rom, Siegfried Müller

Institute for Geometry and Applied Mathematics, RWTH Aachen University, Templergraben 55, 52062 Aachen, Germany

ARTICLE INFO

Keywords:
Hydrodynamic lubrication
Reynolds equation
Elrod–Adams cavitation model
Jakobsson–Floberg–Olsson

ABSTRACT

The Elrod–Adams cavitation model is a commonly used model in the theory of lubricated contacts. Two new interpretations of the model are introduced, a fixed point and an optimal control problem, based on an analytical liquid ratio representation and a suitable cost functional, respectively. For both, possible discretizations are proposed. A rigorous convergence analysis, crucial to ensure convergence of solutions of the discretized models to the solution of the continuous Elrod–Adams model, is possible. Two solution algorithms using a finite element method are presented and applied to two numerical journal bearing experiments. A comparison with the Fischer–Burmeister–Newton–Schur algorithm shows a lower cost per iteration and partly a higher accuracy. Depending on the problem, the overall computational cost is also lower.

1. Introduction

Lubricated contacts can be found in a wide variety of machine elements, ranging from bearings over gears to joints. Modeling the viscous flow in between these lubricated contacts has long been subject to the Reynolds equation [1] as a simplification of the nonlinear Navier–Stokes equations. While being easy to solve with a discretization method of choice, the Reynolds equation has the downside of not being able to model cavitation effects, such as the formation of gas bubbles or gas pockets, in the case of diverging surfaces. Since these effects can have a significant impact on the performance and durability of the underlying machine element, a significant effort has gone into modeling cavitation over the past decades.

First approaches consisted of the Gümbel model [2], where pressure values below a certain cavitation pressure are simply set to that cavitation pressure, and the Swift–Stieber (or Reynolds) boundary condition [3,4], where an additional zero pressure gradient is forced at points of film rupture. While these models are relatively easy to solve numerically, they have the disadvantage of not being able to conserve mass of the lubricant. This can lead to large inaccuracies in certain applications, e.g., textured surface lubrication [5]. To ensure conservation of mass, Jakobsson, Floberg and Olsson added a liquid ratio variable to the Reynolds equation and extended the Swift–Stieber boundary condition by an additional condition at points of film reformation [6,7]. Based on these so-called JFO boundary conditions, Elrod and Adams developed a boundary-free cavitation model consisting of a constrained and modified Reynolds equation [8,9]. This model has proven to be a good compromise between accuracy and practicality and has been mathematically well analyzed in terms of existence and uniqueness of solutions [10]. Some modifications of the model have been proposed, considering both gaseous and vaporous cavitation [11,12], but the classical Elrod–Adams model remains one of the most used cavitation models in practice.

Due to the nonlinear nature of the Elrod–Adams model, specialized numerical algorithms are required to approximate its solution. Elrod himself used a cavitation index to discretize the mass flux [9], while Bayada et al. introduced an artificial time to utilize a characteristics method [13]. Ausas et al. developed a relaxation-type finite volume algorithm [14] that was later extended to a general finite volume method by Profito et al. [15], whereas Tber used a weak formulation in a mixed form combined with a mixed finite element method [16]. Giacopini et al. reformulated the system as a linear complementary problem [17], opening the door to many new solvers such as the Fischer–Burmeister–Newton–Schur (FBNS) algorithm of Woloszynski et al. [18]. Recently, physics-informed neural networks have been employed to the Elrod–Adams model, promising low computation times at the cost of lacking accuracy control [19–21]. These are only a selection of existing numerical algorithms, see [22,23] for more. All existing solvers so far lack either efficiency, accuracy, or a rigorous mathematical background.

In this paper, we present new perspectives on the Elrod–Adams cavitation model by proposing two new mathematically motivated equivalent interpretations, namely the Characteristic Fixed Point (CFP) interpretation and the Optimal Control Problem (OCP) interpretation. These interpretations are compatible with classical discretization schemes like

* Corresponding author.
E-mail addresses: schultz@igpm.rwth-aachen.de (M. Schultz), hannah.orgassa@rwth-aachen.de (H. Orgassa), rom@igpm.rwth-aachen.de (M. Rom), mueller@igpm.rwth-aachen.de (S. Müller).

https://doi.org/10.1016/j.triboint.2025.110967
Received 25 March 2025; Received in revised form 17 June 2025; Accepted 30 June 2025
Available online 13 July 2025

Finite Element Methods (FEM), Finite Difference Methods (FDM), or Finite Volume Methods (FVM) as well as structured and unstructured grids, creating a foundation for versatile and efficient new solution algorithms. The mathematical background allows for a rigorous convergence analysis of the corresponding discretizations, which is not possible with many other cavitation algorithms. Such an analysis is crucial to ensure convergence of discretized solutions to the continuous solution of the Elrod–Adams model. The CFP interpretation additionally allows for the use of non-stabilized discretization schemes. Cavitation algorithms typically require some form of upwind-stabilized discretization of the underlying Reynolds equation in order to deal with the hyperbolic part of the Elrod–Adams model. This often leads to a loss of accuracy of the discretized solutions, especially when working with FEMs. Due to an intrinsic stabilization, this loss of accuracy is avoided.

The starting point of both interpretations is a solution operator for the unconstrained Reynolds equation, which is used to reformulate the Elrod–Adams system as a one-variable system for the liquid ratio. In case of the CFP interpretation, this operator is coupled with an analytical representation of the liquid ratio obtained by the method of characteristics. This results in a fixed point problem in the liquid ratio variable, which can be solved using a Krasnoselskii–Mann iteration [24]. In case of the OCP interpretation, the solution operator is coupled with a cost functional that penalizes violations of the Elrod–Adams constraints. This leads to a box-constrained optimization problem which, after discretization, can be solved by the L-BFGS-B algorithm [25]. Both the CFP and the OCP interpretations are equipped with numerical solvers based on an FEM and are compared with the well-known FBNS algorithm in terms of efficiency and accuracy for two realistic numerical experiments corresponding to journal bearings under different operating conditions.

The present paper is organized as follows: Section 2 is dedicated to the Reynolds equation and the modeling of cavitation effects by the Elrod–Adams model. In Section 3, we reformulate this model into a fixed point problem and demonstrate how to solve it numerically. Another reformulation into an optimal control problem with corresponding numerical solver is presented in Section 4. Section 5 summarizes the FBNS algorithm, which is then used in Section 6 to validate both the CFP and the OCP interpretation for two numerical experiments. Finally, in Section 7 we give a brief summary of our results along with an outlook on future improvements.

2. Reynolds equation

The two-dimensional Reynolds equation [1] is typically used to describe viscous flows in a gap between two close surfaces in relative motion. In case of a stationary surface and a flat surface moving at velocity $\boldsymbol{u} = (u_1, u_2)$, the classical Reynolds equation reads

$$-\nabla\cdot\left(\frac{\rho h^3}{12\eta}\nabla p\right) = -\nabla\cdot\left(\frac{\rho h}{2}\boldsymbol{u}\right). \tag{1}$$

Here h describes the gap height between the two surfaces, ρ and η are the density and dynamic viscosity of the lubricant, respectively, and p is the lubricant pressure distribution, all defined on a two-dimensional and bounded domain Ω. The equation is typically accompanied by problem-specific boundary conditions such as an ambient pressure p_a or periodicity along parts of the boundary. In order to improve readability of the paper, we do not specify the given boundary conditions and assume the lubricant to be incompressible and isoviscous. This allows us to rescale the pressure p by the factor $\lambda\ell_{\mathrm{ref}}/(6\eta|\boldsymbol{u}|)$, with $\lambda = \ell_{\mathrm{ref}}/L_{\mathrm{ref}}$ being the dimensionless ratio of a suitable small reference length ℓ_{ref} and a suitable large reference length L_{ref}. By further rescaling the gap height function with ℓ_{ref} and the computational domain with L_{ref}, we obtain (1) in a compact dimensionless form

$$-\nabla\cdot\left(h^3\nabla p\right) = -\nabla\cdot(h\boldsymbol{e}) \tag{2}$$

as in [5,10,13], where $\boldsymbol{e} = \boldsymbol{u}/|\boldsymbol{u}|$ describes the normalized velocity direction and is assumed to be constant.

As a linear elliptic partial differential equation (PDE) for p, (2) is well analyzed and, given suitable boundary conditions, can be easily solved by standard numerical methods like Finite Element Methods (FEM), Finite Difference Methods (FDM), or Finite Volume Methods (FVM). The resulting pressure distribution is known as the Sommerfeld solution and exhibits areas of high and low pressure peaks. It is well-known that this solution fails to model realistic pressures in case of diverging surfaces since cavitation phenomena within low pressure regions are not taken into account.

2.1. Elrod–Adams cavitation model

In order to overcome these problems, Elrod and Adams introduced a liquid ratio $0 \le \theta \le 1$ to the Reynolds equation describing the ratio between liquid and gas in gap height direction [8,9]. With $\theta = 0$ and $\theta = 1$ corresponding to gaps solely filled with gas and liquid, respectively, they proposed the constrained Reynolds equation

$$-\nabla\cdot\left(h^3\nabla p\right) = -\nabla\cdot(\theta h\boldsymbol{e}), \tag{3a}$$

$$p \ge 0, \quad 0 \le \theta \le 1, \quad (1-\theta)\,p = 0. \tag{3b}$$

For the sake of clarity, we use the cavitation pressure $p_c = 0$. In case of an arbitrary cavitation pressure, the constraints read $p \ge p_c$ and $(1-\theta)(p-p_c) = 0$. The algorithms presented here can be easily adapted to this case. It can be shown that a weak formulation of the system has a unique solution under reasonable conditions [10].

The Elrod–Adams model (3) represents a boundary-free version of the Jakobsson, Floberg and Olsson (JFO) cavitation model [6,7]. In the original model, the domain Ω is split into a cavitation domain $\Omega_0(p) = \{\boldsymbol{x} \in \Omega \mid p(\boldsymbol{x}) \le 0\}$, where the liquid ratio is free to change, and a pressure domain $\Omega \setminus \Omega_0(p)$, where the pressure is positive. On the boundary $\partial\Omega_0(p)$, the JFO boundary conditions (4c) couple the pressure and the liquid ratio to ensure conservation of mass passing through the interface between full film and cavitation zones. Using these definitions, the cavitation system can be reformulated as a free boundary problem

$$-\nabla\cdot\left(h^3\nabla p\right) = -\nabla\cdot(h\boldsymbol{e}), \qquad \text{in } \Omega\setminus\Omega_0(p), \tag{4a}$$

$$0 = -\nabla\cdot(\theta h\boldsymbol{e}), \qquad \text{in } \Omega_0(p), \tag{4b}$$

$$h^3\frac{\partial p}{\partial n} = (1-\theta)\,h\boldsymbol{e}\cdot\boldsymbol{n}, \quad \text{on } \partial\Omega_0(p), \tag{4c}$$

$$p \ge 0, \quad 0 \le \theta \le 1, \qquad \text{in } \Omega, \tag{4d}$$

where $\boldsymbol{n}$ denotes the outward-pointing normal vector of $\partial\Omega_0(p)$. In case of the stationary Reynolds equation (1), the JFO boundary conditions (4c) coincide with the Swift–Stieber boundary condition [3,4] at points of film rupture, simplifying to

$$\frac{\partial p}{\partial n} = 0, \quad \theta = 1, \quad \text{on} \quad \partial\Omega_0^-(p) = \left\{\boldsymbol{x} \in \partial\Omega_0(p) \mid \boldsymbol{e}\cdot\boldsymbol{n}(\boldsymbol{x}) < 0\right\}. \tag{5}$$

A sketch of the free boundary problem (4) is given in Fig. 1. What at first glance looks like two coupled linear PDEs turns out to be a nonlinear and constrained system of equations due to the pressure dependency of the cavitation domain $\Omega_0(p)$. Consequently, specialized numerical methods are required to approximate the solutions.

3. New interpretation I: Characteristic fixed point problem

The first interpretation we present makes us of the free boundary formulation (4). By combining a solution operator for the unconstrained Elrod–Adams equation (3a) with an analytical representation of the liquid ratio solution of (4b), we reformulate the Elrod–Adams model (3) into a fixed point problem in the liquid ratio θ. This problem can then be solved numerically by a Krasnoselskii–Mann iteration [24] and a standard discretization method.

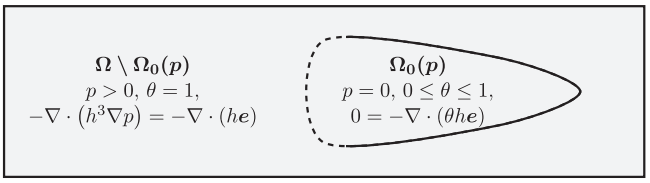

Fig. 1. Sketch of the free boundary problem (4) for $\boldsymbol{e} = (1,0)^\intercal$. The dashed line marks the points of film rupture $\partial\Omega_0^-(p)$, while the solid line marks the points of film reformation.

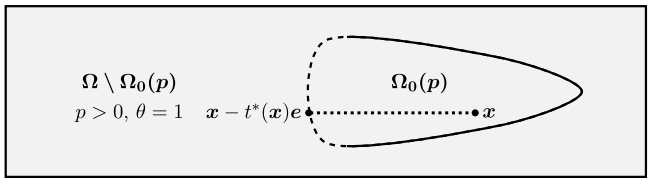

Fig. 2. Sketch of the characteristic approach for $\boldsymbol{e} = (1,0)^\intercal$. The dashed line marks the points of film rupture $\partial\Omega_0^-(p)$, while the solid line marks the points of film reformation.

3.1. Solution operators

For a fixed liquid ratio θ, we can interpret (3a) as a linear elliptic PDE for the pressure p. It is well known that equations of this type admit a unique weak solution given a reasonable right-hand side and boundary conditions. Therefore, we are able to define a solution operator that maps a liquid ratio θ to the corresponding weak pressure solution p via

$$\mathcal{P}(\theta) \begin{cases} \text{For given liquid ratio } \theta \text{ find a pressure } p \text{ such that} \\ \qquad -\nabla \cdot \left(h^3 \nabla p\right) = -\nabla \cdot (\theta h \boldsymbol{e}), \quad \text{in } \Omega. \end{cases} \tag{6}$$

Solutions of $\mathcal{P}(\theta)$ for an arbitrary liquid ratio θ in general do not fulfill the conditions $p \ge 0$ or $(1-\theta)p = 0$. However, assuming that a solution of the Elrod–Adams model (3) is given by (p^*, θ^*), we know that the pressure solution operator fulfills $\mathcal{P}(\theta^*) = p^*$ with $p^* \ge 0$ and $(1-\theta^*)p^* = 0$.

Similarly, we can fix the pressure p and view (4b) and (4c) as an unconstrained hyperbolic PDE system for the liquid ratio θ inside the cavitation domain $\Omega_0(p)$. Systems of these forms are also well analyzed and admit a unique weak solution if the boundary conditions on the outflow part of the boundary $\partial\Omega_0(p) \setminus \partial\Omega_0^-(p)$ are neglected. This allows us to define a solution operator for the liquid ratio θ by

$$C(p) \begin{cases} \text{For given pressure } p \text{ find a liquid ratio } \theta \text{ such that} \\ \qquad \nabla \cdot (\theta h \boldsymbol{e}) = 0, \quad \text{in } \Omega_0(p), \\ \qquad \theta = 1, \quad \text{on } \partial\Omega_0^-(p). \end{cases} \tag{7}$$

Solutions of $C(p)$ for an arbitrary pressure distribution p will in general not fulfill the ratio property $\theta \le 1$ or the JFO boundary conditions (4c). However, analogously to before, the operator fulfills $C(p^*) = \theta^*$ with $0 \le \theta^* \le 1$ and the JFO boundary conditions.

A classical method for solving systems of this form is the method of characteristics, where the solution is determined along traces of particles, called characteristics. We refer to [26] for more details. For our case of a constant vector $\boldsymbol{e}$ and a vanishing right-hand side, the characteristics reduce to straight lines in direction of $\boldsymbol{e}$, along which the quantity θh remains constant. This can also be derived by rewriting the vanishing divergence $\nabla \cdot (\theta h \boldsymbol{e}) = 0$ into a vanishing directional derivative $\boldsymbol{e} \cdot \nabla(\theta h) = 0$. The inflow boundary condition determines the constant along a characteristic. Hence, we obtain an analytical representation of θ that holds on the entire domain Ω

$$\theta(\boldsymbol{x}) = \frac{h(\boldsymbol{x} - t^*(\boldsymbol{x})\boldsymbol{e})}{h(\boldsymbol{x})} \quad \text{with} \quad t^*(\boldsymbol{x}) = \inf\left\{ t \in \mathbb{R}_+ \mid p(\boldsymbol{x} - t\boldsymbol{e}) > 0 \right\}. \tag{8}$$

Depending on the shape of the domain $\Omega_0(p)$, a solution to $C(p)$ can only be found in the weak sense that the derivative of the quantity θh exists in direction of $\boldsymbol{e}$. The analytical representation (8) still applies in this case. A sketch of the characteristic approach is given in Fig. 2.

3.2. The fixed point problem

We now make use of the fact that solutions (p^*, θ^*) of the Elrod–Adams model (3) are mapped onto each other by the operators $\mathcal{P}(\theta^*)$ and $C(p^*)$. This allows us to reformulate the Elrod–Adams model into a fixed point problem for the liquid ratio variable θ by defining the operator

$$T(\theta) := \min\{C(\mathcal{P}(\theta)), 1\}. \tag{9}$$

The liquid ratio θ^* then fulfills the fixed point equation

$$T(\theta^*) = \theta^*. \tag{10}$$

The ratio property $\theta \le 1$ is enforced directly by cutting off the solutions to $C(\mathcal{P}(\theta))$. In this way, fixed points violating the ratio property are avoided. For the one-dimensional case it can be shown that for every fixed point $T(\theta) = \theta$ the pair $(\mathcal{P}(\theta), \theta)$ solves the Elrod–Adams model (3), see Appendix A. A similar result for the two-dimensional case has not yet been obtained.

Solutions of the fixed point problem (10) can now be approximated by a Krasnoselskii–Mann iteration [24], which can be seen as a generalization of the classical Banach fixed point iteration for non-expansive operators. Given a sequence of relaxation parameters $\lambda^k \in (0,1)$, we construct a sequence of liquid ratios θ^k with corresponding pressure distributions $p^k = \mathcal{P}(\theta^k)$ by setting

$$\theta^{k+1} = (1-\lambda^k)\theta^k + \lambda^k T(\theta^k). \tag{11}$$

A typical choice for the relaxation parameters is $\lambda^k = 1/(k+1)$, which corresponds to taking the mean of all operator evaluations $T(\theta^k)$. However, other choices are possible as well, e.g., $\lambda^k = 1/(\alpha k + 1)$ for a constant $\alpha \in (0,1]$.

3.3. Numerical discretization

Discretizing the operator T for the use of (11) in practical applications narrows down to discretizing the subproblems $\mathcal{P}(\theta)$ and $C(p)$. Possible methods for this case are FEMs, FDMs, or FVMs. To keep things general and clear, we use a discretization-independent notation and define $\boldsymbol{p}, \boldsymbol{\theta} \in \mathbb{R}^N$ as the degrees of freedom (DoFs) for p and θ corresponding to any of these methods. The discretization of the pressure problem $\mathcal{P}(\theta)$ now reads

$$\mathcal{P}_\Delta(\boldsymbol{\theta}) \begin{cases} \text{For given } \boldsymbol{\theta} \in \mathbb{R}^N \text{ find } \boldsymbol{p} \in \mathbb{R}^N \text{ such that} \\ \qquad \mathbf{A}\boldsymbol{p} = \mathbf{B}\boldsymbol{\theta} + \boldsymbol{c}. \end{cases} \tag{12}$$

Here, the matrix $\mathbf{A}$ approximates the Poiseuille terms of the unconstrained cavitation system, $\mathbf{B}$ the Couette terms, and the vector $\boldsymbol{c}$ collects the boundary conditions. An example for the matrices $\mathbf{A}$, $\mathbf{B}$ and the vector $\boldsymbol{c}$ in case of an FEM can be found in Appendix B. Evaluating $\mathcal{P}_\Delta(\boldsymbol{\theta})$ now requires solving a linear system of equations with matrix $\mathbf{A}$. Since $\mathcal{P}_\Delta(\boldsymbol{\theta})$ needs to be evaluated in each iteration of (11), it is recommended to calculate an inverse or sparse decomposition of $\mathbf{A}$ at the beginning of the algorithm to significantly reduce the effort per iteration of the algorithm.

For the discretization of $C(p)$ the analytical solution (8) is utilized. Values for the DoFs $\boldsymbol{\theta}$ can be obtained by pointwise interpolation of the analytical solution for the discretized pressure $\boldsymbol{p}$

$$C_\Delta(\boldsymbol{p}) \begin{cases} \text{For given } \boldsymbol{p} \in \mathbb{R}^N \text{ find } \boldsymbol{\theta} \in \mathbb{R}^N \text{ such that} \\ \qquad \theta_i = \dfrac{h(\boldsymbol{x}_i - t_i^* \boldsymbol{e})}{h(\boldsymbol{x}_i)} \text{ for all } i = 1, \dots, N \\ \qquad \text{with } t_i^* = \inf\left\{ t \in \mathbb{R}_+ \mid p(\boldsymbol{x}_i - t\boldsymbol{e}) > 0 \right\}. \end{cases} \tag{13}$$

Here $\boldsymbol{x}_i$ describes the coordinate of the i-th degree of freedom and $p(\cdot)$ a method-specific evaluation of the pressure approximation corresponding to the DoFs $\boldsymbol{p}$. Finding the actual values of t_i^* in (13) can be realized in multiple ways. We either start at the point $\boldsymbol{x}_i$ and run back stepwise in direction of $\boldsymbol{e}$ until the pressure evaluation is positive, or we choose a grid aligned to $\boldsymbol{e}$ and run from DoF to DoF forward in direction of $\boldsymbol{e}$, checking the corresponding pressure sign. The latter approach is preferred for performance reasons. However, both strategies can easily be parallelized, leaving the evaluation of $\mathcal{P}_\Delta(\theta)$ as the bottleneck per iteration.

As a stopping criterion for the fixed point iteration we choose the relative error of the constraint $\boldsymbol{p} \geq \boldsymbol{0}$. Numerical experiments have shown that the expression $\left|\min \boldsymbol{p}^k / \max \boldsymbol{p}^k\right|$ tends to fall to zero and eventually stagnates at a value closely related to the resolution of the cavitation domain. Therefore, for a practical implementation, it is recommended to add a maximal number of iterations or a function that checks for convergence of $\left|\min \boldsymbol{p}^k / \max \boldsymbol{p}^k\right|$. If no information about the liquid ratio is known beforehand, $\boldsymbol{\theta}^0 = \boldsymbol{1}$ can be used as a general initial guess. The resulting algorithm is given by Algorithm 1.

Algorithm 1 The CFP algorithm

Input: Initial liquid ratio $\boldsymbol{\theta}^0 \in \mathbb{R}^N$, relaxation parameters $\lambda^k \in (0,1)$, stopping criterion $\varepsilon > 0$

Output: Pressure and liquid ratio approximations $\boldsymbol{p}, \boldsymbol{\theta} \in \mathbb{R}^N$

Solve $\mathcal{P}_\Delta(\boldsymbol{\theta}^0)$ for $\boldsymbol{p}^0$
Set $k = 0$
while $\left|\min \boldsymbol{p}^k / \max \boldsymbol{p}^k\right| \geq \varepsilon$ **do**
    Solve $C_\Delta(\boldsymbol{p}^k)$ for $\widetilde{\boldsymbol{\theta}}^k$
    Set $\boldsymbol{\theta}^{k+1} = (1-\lambda^k)\boldsymbol{\theta}^k + \lambda^k \min\left\{\widetilde{\boldsymbol{\theta}}^k, \boldsymbol{1}\right\}$
    Solve $\mathcal{P}_\Delta(\boldsymbol{\theta}^{k+1})$ for $\boldsymbol{p}^{k+1}$
    Set $k = k+1$
end while

4. New interpretation II: Optimal control problem

The second interpretation we present is the optimal control problem interpretation. By introducing a cost functional that penalizes violations of the complementary constraints (3b), we reformulate the Elrod–Adams model (3) into an optimal control problem in the liquid ratio θ. This problem can then be solved numerically using a standard discretization method and the L-BFGS-B algorithm [25].

4.1. Optimal control problem

In the Elrod–Adams model (3), the pressure and cavitation variables are coupled by the PDE (3a) while also being subject to multiple constraints (3b). This setting is frequently found in the field of optimal control [27], which motivates us to interpret the given system as an optimal control problem. Problems of this type typically consist of a control variable, which acts as an input to the system, and a state that can be seen as a response of the system. An optimal control is then given by a control variable that minimizes a specified cost functional with its state. In case of the Elrod–Adams model, the liquid ratio θ functions as a constrained control variable and the corresponding pressure $p = \mathcal{P}(\theta)$ as a state. The optimal control problem then reads

$$\begin{aligned} &\min\ J(p,\theta) \\ &\text{s.t.} -\nabla\cdot\left(h^3\nabla p\right) = -\nabla\cdot(\theta h \boldsymbol{e}), \\ &\qquad 0 \leq \theta \leq 1, \end{aligned} \tag{14}$$

where $J(p,\theta)$ is an appropriate cost functional, to be minimized. In order to account for the remaining complementary constraints $p \geq 0$ and $(1-\theta)p = 0$, we define the cost functional as

$$J(p,\theta) = \frac{1}{2}\int_\Omega ((1-\theta)p)^2\,\mathrm{d}\boldsymbol{x} + \frac{1}{2}\int_\Omega \min(0,p)^2\,\mathrm{d}\boldsymbol{x}. \tag{15}$$

By definition, $J(p,\theta)$ is minimal if the constraints $p \geq 0$ and $(1-\theta)p = 0$ are fulfilled. Consequently, the optimal control problem (14) and the Elrod–Adams model (3) are equivalent.

Inserting the solution operator $\mathcal{P}(\theta)$ into the optimal control problem (14) leads to a reduced system in which the PDE is dropped, as it is contained in $\mathcal{P}(\theta)$. The new system depends only on the control θ and is given by

$$\begin{aligned} &\min\ \hat{J}(\theta) = J(\mathcal{P}(\theta),\theta) \\ &\text{s.t. } 0 \leq \theta \leq 1. \end{aligned} \tag{16}$$

Existence and uniqueness of solutions to this system are a direct consequence of the existence and uniqueness of solutions to the Elrod–Adams model (3). Note that the cost functional (15) is not the only possible choice to reformulate the Elrod–Adams model. In fact, there might be a more suitable cost functional to describe the problem that can prevent local minimizers in case of a strictly convex functional.

4.2. Numerical discretization

In order to solve problem (16) numerically, we make use of the discretized solution operator $\mathcal{P}_\Delta(\theta)$ introduced in Section 3.3. Using the DoF vectors $\boldsymbol{p}, \boldsymbol{\theta} \in \mathbb{R}^N$, it can be written as

$$\boldsymbol{p} = \mathcal{P}_\Delta(\boldsymbol{\theta}) = \boldsymbol{A}^{-1}(\boldsymbol{B}\boldsymbol{\theta} + \boldsymbol{c}). \tag{17}$$

The cost functional $\hat{J}(\theta)$ can then be discretized by approximating the integrals on the grid points of the discretization. For a grid consisting of rectangular cells with edge sizes Δx_1 and Δx_2, this leads to the discretized cost functional

$$\hat{J}_\Delta(\boldsymbol{\theta}) = \frac{\Delta x_1 \Delta x_2}{2}\left(\mathcal{P}_\Delta(\boldsymbol{\theta})^2 \cdot (\boldsymbol{1}-\boldsymbol{\theta})^2 + \min\left(\boldsymbol{0}, \mathcal{P}_\Delta(\boldsymbol{\theta})\right)\cdot\min\left(\boldsymbol{0}, \mathcal{P}_\Delta(\boldsymbol{\theta})\right)\right), \tag{18}$$

where the square and minimum are applied componentwise to the vectors, and '$\cdot$' denotes the inner product. The resulting discretized reduced control problem reads

$$\begin{aligned} &\min\ \hat{J}_\Delta(\boldsymbol{\theta}) \\ &\text{s.t. } \boldsymbol{0} \leq \boldsymbol{\theta} \leq \boldsymbol{1} \in \mathbb{R}^N. \end{aligned} \tag{19}$$

This is a constrained optimization problem in $N \gg 1$ variables and can be solved with any suitable optimization algorithm. Since the discretized cost functional is differentiable, we are able to use gradient-based algorithms like the L-BFGS-B algorithm [25], which is an extension of the quasi-Newton L-BFGS algorithm [28] to box-constrained problems. We refer to [25] for details on the L-BFGS-B algorithm. One detail we would like to point out, however, is that the L-BFGS-B algorithm requires one evaluation of the cost functional $\hat{J}_\Delta(\boldsymbol{\theta})$ as well as one evaluation of its gradient $\nabla\hat{J}_\Delta(\boldsymbol{\theta})$ per iteration. The corresponding gradient is given by

$$\begin{aligned} \nabla\hat{J}_\Delta(\boldsymbol{\theta}) &= \Delta x_1 \Delta x_2 \\ &\times \left(\left(\mathbf{A}^{-\mathbf{1}}\mathbf{B}\right)^{\mathrm{T}}\left(\mathcal{P}_\Delta(\boldsymbol{\theta}) : (\boldsymbol{1}-\boldsymbol{\theta})^2 + \min\left(\boldsymbol{0}, \mathcal{P}_\Delta(\boldsymbol{\theta})\right)\right) - (\boldsymbol{1}-\boldsymbol{\theta}) : \mathcal{P}_\Delta(\boldsymbol{\theta})^2\right), \end{aligned} \tag{20}$$

where the square and minimum are again applied componentwise, and '$:$' denotes a componentwise multiplication. Since the gradient evaluation also involves an evaluation of the inverse matrix $\mathbf{A}^{-\mathbf{1}}$, the effort per iteration is roughly given by the cost of solving two linear systems of equations. Therefore, performing a sparse matrix decomposition of $\mathbf{A}$ at the beginning of the algorithm is again highly recommended. If no information about the liquid ratio is known beforehand, $\boldsymbol{\theta}^0 = \boldsymbol{1}$ can

again be used as a general initial guess. An implementation of the OCP algorithm is summarized in Algorithm 2.

Algorithm 2 The OCP algorithm

Input: Initial liquid ratio $\theta^0 \in \mathbb{R}^N$, stopping criterion $\varepsilon > 0$

Output: Pressure and liquid ratio approximations $p, \theta \in \mathbb{R}^N$

Solve $\mathcal{P}_\Delta(\theta^0)$ for p^0
Set $\hat{J}_\Delta^{-1} = 0$
Set $\hat{J}_\Delta^0 = \hat{J}_\Delta(\theta^0)$
Set $k = 0$
while $|\hat{J}_\Delta^{k-1} - \hat{J}_\Delta^k| \,/\, \max\left(1, |\hat{J}_\Delta^{k-1}|, |\hat{J}_\Delta^k|\right) \geq \varepsilon$ **do**
    Set $\hat{J}_\Delta^k = \hat{J}_\Delta(\theta^k)$
    Set $\nabla \hat{J}_\Delta^k = \nabla \hat{J}_\Delta(\theta^k)$
    Perform L-BFGS-B step for θ^{k+1}
    Solve $\mathcal{P}_\Delta(\theta^{k+1})$ for p^{k+1}
    Set $k = k + 1$
end while

5. FBNS algorithm

In order to validate the CFP and OCP algorithm, we compare their results to the results of the well-known Fischer–Burmeister–Newton–Schur (FBNS) algorithm, developed by Woloszynski et al. in [18]. Its main idea is to view the discretized system (12) as a linear complementarity problem (LCP) and to make use of Fischer–Burmeister functions to reformulate it as an unconstrained system of nonlinear equations. Solutions of the unconstrained system are then iteratively approximated by Newton's method, resulting in a linear system of equations per iteration. This is solved by first performing smart column permutations and then using the Schur complement to reduce the size of the system to be solved. In the following we give a short overview of the algorithm and refer to [18] for further details.

5.1. Linear complementarity problem

In contrast to the newly introduced algorithms in Sections 3 and 4, the FBNS algorithm is not based on the continuous Elrod–Adams cavitation model (3) but on the already discretized system (12). By introducing an inverted liquid ratio $\boldsymbol{\Theta} := \mathbf{1} - \boldsymbol{\theta}$ and neglecting the condition $\boldsymbol{\theta} \geq \mathbf{0}$, the system can be rewritten into a linear complementarity problem (LCP)

$$\boldsymbol{G}(\boldsymbol{p}, \boldsymbol{\Theta}) := \boldsymbol{A}\boldsymbol{p} + \boldsymbol{B}(\boldsymbol{\Theta} - \mathbf{1}) - \boldsymbol{c} = \mathbf{0}, \quad \boldsymbol{p}, \boldsymbol{\Theta} \geq \mathbf{0}, \quad \boldsymbol{p} \cdot \boldsymbol{\Theta} = 0. \tag{21}$$

A common approach to solve LCPs is to make use of Newton-based methods. In these methods, the complementary constraints are dealt with by introducing a Fischer–Burmeister function for each DoF

$$F_i(p_i, \Theta_i) := p_i + \Theta_i - \sqrt{p_i^2 + \Theta_i^2}, \quad i = 1, \dots, N. \tag{22}$$

These functions have the special property, that $\boldsymbol{F}(\boldsymbol{p}, \boldsymbol{\Theta}) = \mathbf{0}$ if and only if $\boldsymbol{p}, \boldsymbol{\Theta} \geq \mathbf{0}$ and $\boldsymbol{p} \cdot \boldsymbol{\Theta} = 0$, while being differentiable on $\mathbb{R}^2 \setminus \{(0,0)\}$. By replacing the complementary constraints for the Fischer–Burmeister functions, the LCP (21) is turned into an unconstrained system of nonlinear equations

$$\boldsymbol{H}(\boldsymbol{p}, \boldsymbol{\Theta}) := \begin{bmatrix} \boldsymbol{F}(\boldsymbol{p}, \boldsymbol{\Theta}) \\ \boldsymbol{G}(\boldsymbol{p}, \boldsymbol{\Theta}) \end{bmatrix} = \mathbf{0}. \tag{23}$$

5.2. Solution procedure

An important property of the system (23) is the differentiability of the function $\boldsymbol{H}(\boldsymbol{p}, \boldsymbol{\Theta})$ almost everywhere in $\mathbb{R}^N \times \mathbb{R}^N$. This allows for the use of gradient-based root-finding algorithms. In the case of the FBNS algorithm, Newton's method is used to approximate roots of $\boldsymbol{H}(\boldsymbol{p}, \boldsymbol{\Theta})$. In each step of the method, updates $\delta\boldsymbol{p}^k, \delta\boldsymbol{\Theta}^k \in \mathbb{R}^N$ of the pressure and inverse liquid ratio are calculated by solving the linear system of equations

$$\boldsymbol{J}_{\boldsymbol{H}}^k \begin{bmatrix} \delta\boldsymbol{p}^k \\ \delta\boldsymbol{\Theta}^k \end{bmatrix} = -\boldsymbol{H}^k, \quad \begin{bmatrix} \boldsymbol{p}^{k+1} \\ \boldsymbol{\Theta}^{k+1} \end{bmatrix} = \begin{bmatrix} \boldsymbol{p}^k + \delta\boldsymbol{p}^k \\ \boldsymbol{\Theta}^k + \delta\boldsymbol{\Theta}^k \end{bmatrix}. \tag{24}$$

The corresponding matrix $\mathbf{J}_{\boldsymbol{H}}^k$ is given by the Jacobian of the system (23), which can be written as

$$\boldsymbol{J}_{\boldsymbol{H}}(\boldsymbol{p}, \boldsymbol{\Theta}) = \begin{bmatrix} \mathbf{J}_{\boldsymbol{F},\boldsymbol{p}} & \mathbf{J}_{\boldsymbol{F},\boldsymbol{\Theta}} \\ \boldsymbol{A} & \boldsymbol{B} \end{bmatrix}. \tag{25}$$

Here, the matrices $\mathbf{J}_{\boldsymbol{F},\boldsymbol{p}}$ and $\mathbf{J}_{\boldsymbol{F},\boldsymbol{\Theta}}$ collect the derivatives of the Fischer–Burmeister functions, leading to two diagonal matrices with entries

$$\left(\mathbf{J}_{\boldsymbol{F},\boldsymbol{p}}\right)_{ii}(\boldsymbol{p}, \boldsymbol{\Theta}) := 1 - \frac{p_i}{\sqrt{p_i^2 + \Theta_i^2}}, \quad \left(\mathbf{J}_{\boldsymbol{\Theta},\boldsymbol{p}}\right)_{ii}(\boldsymbol{p}, \boldsymbol{\Theta}) := 1 - \frac{\Theta_i}{\sqrt{p_i^2 + \Theta_i^2}}. \tag{26}$$

Due to the block structure of the Jacobian $\mathbf{J}_{\boldsymbol{H}}$, the system (24) can be efficiently solved by using the Schur complement after smart column swapping. This effectively reduces the system size from $2N$ unknowns to N unknowns. We refer to [18] for further details on how to solve the system (24) efficiently. A drawback of the column swapping is that in each iteration of the algorithm a new linear system of equations has to be solved. This prohibits the use of sparse decompositions, making the FBNS algorithm more costly per iteration than the CFP and OCP algorithm. If no information about the pressure and liquid ratio solutions is known beforehand, $\boldsymbol{p}^0 = \mathbf{0}$ and $\boldsymbol{\Theta}^0 = \mathbf{0}$ can be used as general initial guesses. The full FBNS algorithm is given by Algorithm 3.

Algorithm 3 The FBNS algorithm

Input: Initial values $\boldsymbol{p}^0, \boldsymbol{\Theta}^0 \in \mathbb{R}^N$, stopping criterion $\varepsilon > 0$

Output: Pressure and inverse liquid ratio approximations $\boldsymbol{p}, \boldsymbol{\Theta} \in \mathbb{R}^N$

Set $\boldsymbol{H}^0 = \boldsymbol{H}(\boldsymbol{p}^0, \boldsymbol{\Theta}^0)$
Set $\delta\boldsymbol{p}^0 = \mathbf{0}$
Set $\delta\boldsymbol{\Theta}^0 = \mathbf{0}$
Set $k = 0$
while $\max\left\{\|\boldsymbol{H}^k\|_\infty, \|\delta\boldsymbol{p}^k\|_\infty, \|\delta\boldsymbol{\Theta}^k\|_\infty\right\} \geq \varepsilon$ **do**
    Set $\boldsymbol{J}_{\boldsymbol{H}}^k = \boldsymbol{J}_{\boldsymbol{H}}(\boldsymbol{p}^k, \boldsymbol{\Theta}^k)$
    Set $\boldsymbol{H}^k = \boldsymbol{H}(\boldsymbol{p}^k, \boldsymbol{\Theta}^k)$
    Solve $\boldsymbol{J}_{\boldsymbol{H}}^k \begin{bmatrix} \delta\boldsymbol{p}^k \\ \delta\boldsymbol{\Theta}^k \end{bmatrix} = -\boldsymbol{H}^k$ for $\delta\boldsymbol{p}^k, \delta\boldsymbol{\Theta}^k$
    Set $\boldsymbol{p}^{k+1} = \boldsymbol{p}^k + \delta\boldsymbol{p}^k$
    Set $\boldsymbol{\Theta}^{k+1} = \boldsymbol{\Theta}^k + \delta\boldsymbol{\Theta}^k$
    Set $k = k + 1$
end while

6. Numerical experiments

In this section, we validate the CFP and OCP algorithm against the FBNS algorithm for two two-dimensional test cases with realistic physical parameters, see Table 1. These correspond to journal bearings under different operating conditions, namely an eccentric journal bearing with high rotational velocity and a misaligned journal bearing with lower rotational velocity. Assuming that the bearings can be unfolded

Table 1
List of parameters for the eccentric and misaligned journal bearing.

	Variable	Eccentric	Misaligned	Unit
Unfolded length	L	0.15	0.08	m
Width	W	0.03	0.02	m
Oil supply length	L_s	6	3.2	mm
Oil supply width	W_s	6	4	mm
Radial clearance	c	30	25	μm
Relative eccentricity	ε_{rel}	0.6	0.8	–
Rotational velocity	$\boldsymbol{u}$	(6, 0)	(2, 0)	m/s
Dynamic viscosity	η	0.01	0.01	Pa s
Density	ρ	820	820	kg/m^3
Ambient pressure	p_a	0.1	0.1	MPa
Supply pressure	p_s	0.3	0.3	MPa
Cavitation pressure	p_c	0.08	0.08	MPa
Reynolds number	Re	14.76	4.1	–

into a rectangle of length L and width W, the respective geometries are modeled by the gap height functions

$$h_e(\boldsymbol{x}) = c\left(1 + \varepsilon_{rel}\cos(2\pi x_1/L)\right), \tag{27a}$$

$$h_m(\boldsymbol{x}) = c\left(1 + \varepsilon_{rel}\left(1 - 2x_2/W\right)\cos(2\pi x_1/L)\right). \tag{27b}$$

Here, c describes the radial clearance between shaft and housing and ε_{rel} the relative eccentricity of the shaft. The corresponding Reynolds equation is equipped with constant Dirichlet boundary conditions on the lower and upper boundary ($x_2 = 0$, $x_2 = W$), modeling the ambient pressure p_a, as well as periodic boundary conditions on the left and right boundary ($x_1 = 0$, $x_1 = L$). Additionally, a rectangular oil supply of length L_s and width W_s centered at $\boldsymbol{x} = (0, W/2)$ is modeled by imposing a constant supply pressure p_s at all points inside the supply zone. In order to avoid numerical problems coming from the h^3 term, the dimensionless formulation (2) is utilized, where the reference length ℓ_{ref} is chosen as the radial clearance c and the reference length L_{ref} as the length L of the computational domain. After computation the results are dimensionalized again for display.

Remark 6.1. In the following, we assume the ambient pressure p_a to be greater than the cavitation pressure p_c. As a consequence, the oil film is full at the lower and upper boundary and the domain of film rupture is cavitated. However, depending on the use case, real journal bearings can show film rupture domains that extend to the lower and upper boundary. In order to model such effects, further boundary conditions for θ need to be set as the Elrod–Adams model (3) is not well-defined for $p_a = p_c$. These additional boundary conditions need to consider effects like capillarity and surface wetting and are beyond the scope of this paper.

In Sections 6.1 and 6.2, we use an FEM with shape functions of degree 1 and a grid consisting of 800 × 200 cells for the discretization $\mathcal{P}_\Delta(\theta)$. The fine grid ensures a sufficient resolution of the cavitation domain as well as grid-converged results. In order for the OCP and FBNS algorithm to converge, some form of stabilization is required. Therefore, we stabilize the FEM by computing the stiffness matrix $\mathbf{B}$ with an upwind quadrature similar to the one used in [29] instead of the usual Gauß-Lobatto quadrature. We refer to Appendix B for more details on the FEM discretization and the stabilization. As initial guess for the algorithms we use $\boldsymbol{\theta}^0 = \mathbf{1}$ and $(\boldsymbol{p}^0, \boldsymbol{\Theta}^0) = (\mathbf{0}, \mathbf{0})$, respectively. Choosing other initial conditions can have positive but also negative impacts on the number of iterations. Even if some rough prior knowledge on the cavitation area is available, this does not necessarily lead to a reduction of the number of iterations. In order to ensure a comparable accuracy of the results, the corresponding stopping criteria are chosen as $\varepsilon_C = 5 \cdot 10^{-4}$ for the CFP algorithm, $\varepsilon_O = 1 \cdot 10^{-4}$ for the OCP algorithm, and $\varepsilon_F = 1 \cdot 10^{-10}$ for the FBNS algorithm. The relaxation parameters of the CFP algorithm are chosen as $\lambda^k = 1/(\alpha k + 1)$ with $\alpha = 0.66$ in all experiments. This choice is motivated by parameter studies performed in Sections 6.1 and 6.2, see Tables 2 and 3, respectively.

All algorithms are implemented in C++ using the software libraries deal.II [30] and LBFGS++ [31] for the FEM and L-BFGS-B algorithm, respectively. The implementation is generally serial, but some parts of the deal.II library, like vector additions or matrix vector multiplications, run thread-parallel. The linear systems are solved by applying a sparse matrix decomposition performed by the UMFPACK [32]. In case of the CFP and OCP algorithms, this routine is called once in the beginning, while for the FBNS algorithm it is called in every iteration. All experiments are performed on a workstation with an Intel Core i7-12700H Processor at 4.70 GHz and 32 GB RAM.

6.1. Eccentric journal bearing

In case of the eccentric journal bearing, the CFP algorithm reaches the given tolerance after 196 iterations with the results depicted in Fig. 3. In contrast, the OCP algorithm needs 2442 iterations, while the FBNS algorithm reaches the given tolerance after only 28 iterations. In Section 6.4, we discuss how this affects the total runtime of the algorithms. Concerning the quality, all results are almost identical with some slight differences around the cavitation domain boundary, as can be seen in Fig. 4, where the absolute differences of the CFP and OCP results with respect to the FBNS reference solution are plotted. The CFP algorithm tends to underestimate the liquid ratio at the outflow part of the cavitation domain, resulting in small inaccuracies of the pressure in this region. Additionally, the pressure inside the cavitation domain is always slightly negative, supporting the analytical liquid ratio approach. Contrarily to the CFP algorithm, the OCP algorithm tends to overestimate the pressure around the inflow part of the cavitation domain boundary. All inaccuracies are only minor though and decrease with the number of iterations. A line plot along the centerline $x_2 = 0.015\,\text{m}$ furthermore confirms the accuracy of the CFP and OCP solutions, see Fig. 5.

It is worthwhile mentioning that the choice of the relaxation constant $\alpha \in (0, 1]$ has a significant impact on the convergence speed of the CFP algorithm. As can be seen in Table 2, smaller constants α drastically reduce the number of necessary iterations since larger liquid ratio updates are performed in each step of the algorithm. However, choosing α too small can lead to instabilities and failure of the Krasnoselskii–Mann iteration. An optimal choice for α seems to be problem-dependent.

6.2. Misaligned journal bearing

In case of the misaligned journal bearing, the OCP algorithm reaches the given tolerance after 1858 iterations with the results depicted in Fig. 6. The CFP algorithm needs 257 iterations, while the FBNS algorithm reaches the tolerance after 24 iterations. Concerning the quality, all algorithms handle the disjoint cavitation domains equally well and lead to similar results. The main differences, as can be seen in Fig. 7, are located again around the boundary of the cavitation domain, where the CFP algorithm slightly underestimates the liquid ratio at

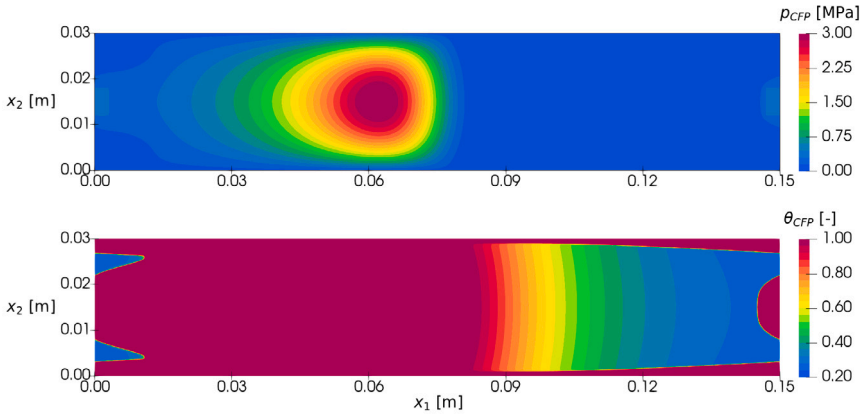

Fig. 3. Pressure and liquid ratio output of the CFP algorithm for the eccentric journal bearing.

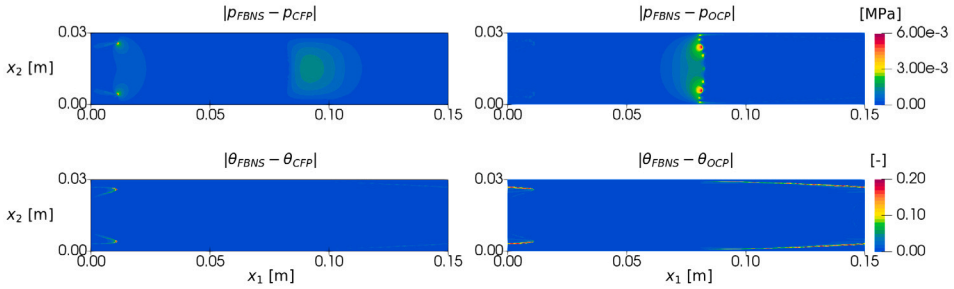

Fig. 4. Absolute differences between the pressure and liquid ratio outputs of the CFP/OCP algorithm and the FBNS algorithm for the eccentric journal bearing.

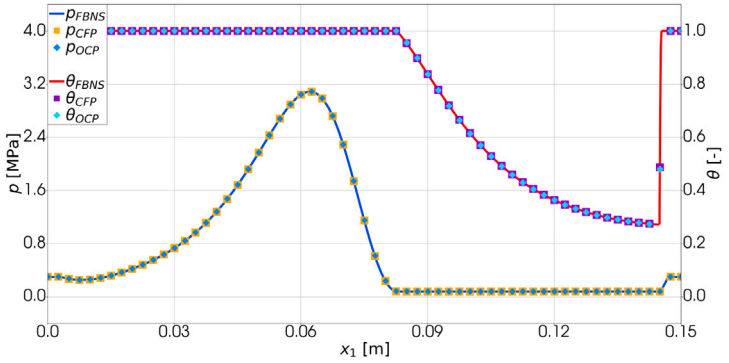

Fig. 5. Pressure and liquid ratio outputs at $x_2 = 0.015\,\mathrm{m}$ for the eccentric journal bearing.

Table 2
Number of iterations of the CFP algorithm for different relaxation constants α for the eccentric journal bearing.

α	1	0.8	0.6	0.4	0.2	0
Iterations	1301	414	158	151	166	–

the outflow boundary as well as the pressure inside the cavitation domain and the OCP algorithm slightly overestimates the pressure at the inflow boundary. A line plot along $x_2 = 0.003\,\mathrm{m}$, see Fig. 8, furthermore verifies the accuracy of the CFP and OCP solutions. The iteration behavior of the CFP algorithm depends again significantly on the relaxation constant α, see Table 3. Choosing α too large results in a high number of iterations, while choosing α too small introduces instabilities.

6.3. Stabilization impact

In order to visualize the impact of the upwind quadrature on the discretization error made with $\mathcal{P}_\Delta(\theta)$, we run the previous experiments for various uniform refinements of a 100×25 grid and compare the results of the stabilized discretization $\mathcal{P}_\Delta(\theta)$, obtained by the OCP and FBNS algorithm, to the ones of the non-stabilized discretization $\mathcal{P}^*_\Delta(\theta)$, obtained by the CFP algorithm. The initial grid is chosen such that the oil supply boundaries are exactly captured, minimizing any effects coming from an unresolved oil supply. The algorithm settings are identical to the previous experiments with the only exception of a stopping criterion of $\varepsilon_C = 3 \cdot 10^{-3}$ for the CFP algorithm due to an earlier stagnation of $\left|\min \boldsymbol{p}^k / \max \boldsymbol{p}^k\right|$. For comparison, we calculate a set of performance parameters and investigate their convergence. These parameters are chosen as the maximal pressure $p_{\max}$, the load-carrying capacity W, the friction force F, and the side leakage Q, which are

Table 3
Number of iterations of the CFP algorithm for different relaxation constants α for the misaligned journal bearing.

α	1	0.8	0.6	0.4	0.2	0
Iterations	913	362	312	609	843	–

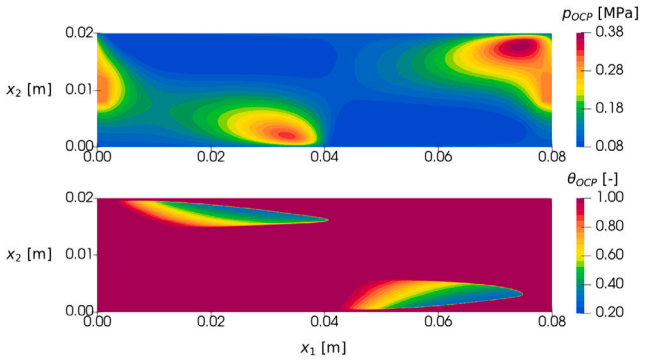

Fig. 6. Pressure and liquid ratio output of the OCP algorithm for the misaligned journal bearing.

given by

$$p_{\max} = \max_{\boldsymbol{x}\in\Omega} p(\boldsymbol{x}), \qquad W = \int_\Omega \max\{p - p_c, 0\}\,\mathrm{d}\boldsymbol{x}, \tag{28}$$

$$F = \int_\Omega \frac{h}{2}\frac{\partial p}{\partial x_1} + \frac{\eta u_1}{h}\,\mathrm{d}\boldsymbol{x}, \quad Q = \int_\Gamma \max\left\{-\frac{\rho h^3}{12\eta}\frac{\partial p}{\partial n}, 0\right\}\mathrm{d}S, \tag{29}$$

where Γ denotes the lower and upper boundary of Ω ($x_2 = 0$, $x_2 = W$) and $\boldsymbol{n}$ the outward-pointing normal vector of Γ.

Figs. 9 and 10 show that the performance parameters of both the stabilized and the non-stabilized systems converge to the same values for an increasing number of DoFs N. While the differences of the friction forces F and side leakages Q are only minor, the differences of the maximal pressure $p_{\max}$ and the load-carrying capacity W are more significant. We observe that the non-stabilized performance parameters generally converge faster than the stabilized ones. This allows for the use of coarser grids to achieve a comparable level of accuracy in the performance parameters, significantly boosting the CFP algorithm's runtime. Lastly, we note that the performance parameters computed with the OCP algorithm are almost identical to the ones obtained by the FBNS algorithm, furthermore underlining the accuracy of the OCP algorithm's solutions.

Remark 6.2. The slow convergence of the OCP and the FBNS algorithm is caused by the upwind stabilization of the underlying FEM discretization needed in the discretization of a hyperbolic problem in the cavitation region. In FEMs the upwind stabilization can only be performed up to the cell boundary. Using a finite volume method instead might improve the convergence rate because upwind stabilization can be performed beyond the cell boundary. Due to the exact integration along characteristics the CFP algorithm does not have such a limitation. This shows the superiority of this method in combination with FEM discretizations.

6.4. Computational efficiency

We conclude this numerical section with a few remarks on the computational efficiency of the studied algorithms. Table 4 shows the total CPU times and the CPU times per iteration for the CFP, OCP, and FBNS algorithm in the eccentric and misaligned numerical experiment. As expected, the sparse matrix decomposition drastically accelerates the CPU times per iteration, in case of the OCP algorithm (0.15 s) by a factor of 7 and in case of the CFP algorithm (0.09 s) even by a factor of 10 compared to the FBNS algorithm (1.00 s). For finer grids, this effect is further amplified. This advantage, however, is compensated by the high number of iterations, resulting in a comparable total runtime between the FBNS (31 s and 24 s) and CFP algorithm (19 s and 23 s) and a worse total runtime for the OCP algorithm (377 s and 282 s).

When working with FEMs, making use of the non-stabilized system with coarser grids can also have a large impact on the computational efficiency, depending on the desired accuracy. To achieve a similar accuracy with respect to the performance parameters computed with the CFP algorithm on an 800×200 grid, the FBNS algorithm needs to be run at least on a 3200×800 grid, see Figs. 9 and 10. This slows down the time per iteration to the point that the CFP algorithm is significantly faster in total despite the higher number of iterations, see Table 4. In case of the eccentric bearing the speedup is 64 (700 s to 11 s) and in case of the misaligned bearing, where fewer iterations are required, the speedup is 21 (815 s to 38 s). These significant speedups but also the moderate ones described above (19 s instead of 31 s) are promising for applications which require the repeated computation of the pressure distribution, e.g., (thermo)elastohydrodynamic simulations.

7. Conclusion

In this work, we developed two new interpretations of the Elrod–Adams cavitation model. As these interpretations are independent of the discretization scheme used to solve the Reynolds equation, they form a foundation for new and efficient cavitation algorithms. Their mathematical background allows for a rigorous convergence analysis of the new algorithms, which is crucial to ensure the convergence of discretized solutions to the continuous solution of the Elrod–Adams model. We validated two cavitation algorithms derived from the new interpretations in combination with an FEM against the well-known FBNS algorithm in two realistic numerical experiments. The algorithms showed a comparably high number of iterations but also a lower cost per iteration. In case of the CFP algorithm, the lower cost compensated the high iteration number, resulting in a competitive algorithm. Combined with the higher accuracy for FEMs, the CFP algorithm proved to be interesting for practical applications.

Reducing the CFP and OCP algorithms' iteration numbers to further boost efficiency is an important open topic. In case of the CFP algorithm, this might be possible with a different choice of relaxation parameters λ^k. Not every in the theory of Krasnoselskii–Mann iterations admissible set of relaxation parameters is suitable for the CFP algorithm. Nevertheless, the question remains whether a better choice than $\lambda^k = \frac{1}{\alpha\, k+1}$ can be found. For this purpose, modified Krasnoselskii–Mann iterations may also be of interest. First numerical experiments have shown that inertial Krasnoselskii–Mann iterations [33] have the potential of speeding up the convergence of the CFP algorithm at the cost of adding an additional problem-dependent parameter, which can lead to instabilities if wrongly chosen. For the OCP algorithm, a different cost functional could possibly lower the necessary number of iterations. Moreover, strictly convex cost functionals could also prevent local minimizers, which theoretically lead to a failure of the algorithm. Local minimizers have not been a problem in all of our tested cases though.

From an engineering point of view, an important open topic is the extension of the CFP and OCP interpretation to the transient Reynolds equation. While the OCP algorithm could be used on a standard time discretization, the CFP algorithm's analytical liquid ratio representation needs to be extended to time-dependent gap heights. It is likely that similar efficiency and accuracy results will appear.

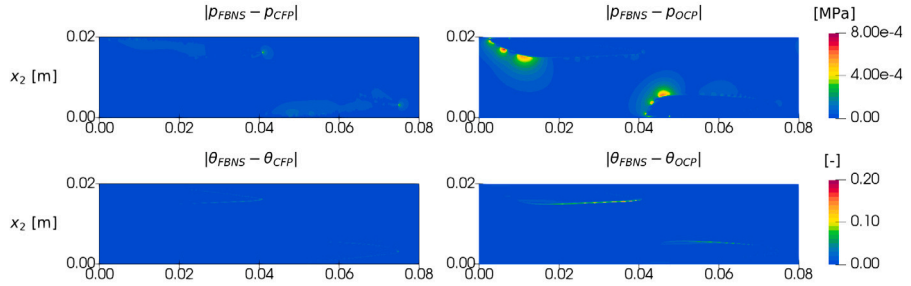

Fig. 7. Absolute differences between the pressure and liquid ratio outputs of the CFP/OCP algorithm and the FBNS algorithm for the misaligned journal bearing.

Table 4
CPU times of the CFP, OCP and FBNS algorithm. CFP* uses the non-stabilized discretization $\mathcal{P}_4^*(\theta)$.

Algorithm	CFP	OCP	FBNS	CFP*	FBNS
Number of cells [–]	800 × 200	800 × 200	800 × 200	800 × 200	3200 × 800
Eccentric					
Number of iterations [–]	196	2442	28	118	32
CPU time [s]	19	377	31	11	700
CPU time per iteration [s]	0.10	0.15	1.11	0.09	21.9
Misaligned					
Number of iterations [–]	257	1858	24	413	38
CPU time [s]	23	282	24	38	815
CPU time per iteration [s]	0.09	0.15	1.00	0.09	21.4

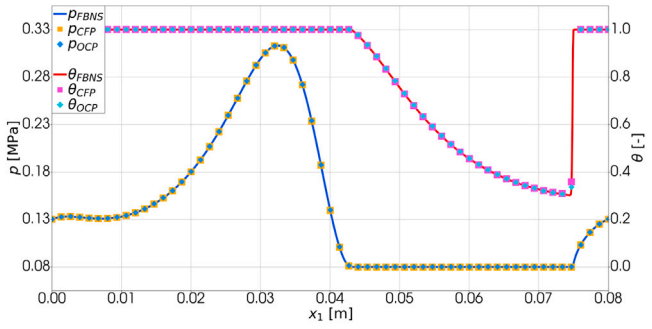

Fig. 8. Pressure and liquid ratio outputs at $x_2 = 0.003\,\mathrm{m}$ for the misaligned journal bearing.

CRediT authorship contribution statement

Matti Schultz: Writing – original draft, Visualization, Validation, Software, Methodology, Investigation, Formal analysis, Data curation, Conceptualization. **Hannah Orgassa:** Writing – original draft, Visualization, Software, Investigation. **Michael Rom:** Writing – review & editing, Conceptualization. **Siegfried Müller:** Writing – review & editing, Supervision, Conceptualization.

Declaration of competing interest

The authors declare that they have no known competing financial interests or personal relationships that could have appeared to influence the work reported in this paper.

Acknowledgments

This work has been supported by the DFG (German Research Foundation) through the project *"Efficient numerical methods for the tribological analysis of textured journal bearing systems"* (project number: 511282384). The authors would like to thank Martin Grepl for sharing his expertise in the field of optimal control problems.

Appendix A

In Section 3 we established that for every solution (p, θ) of the Elrod–Adams model (3) θ is a fixed point of the operator $T(\theta)$. Here we show that, at least in the one-dimensional case, the opposite also holds true, proving the Elrod–Adams model and the fixed point problem to be equivalent.

Theorem 1. *Let the dimension be $d = 1$. For every fixed point $\theta = T(\theta)$ the pair $(\mathcal{P}(\theta), \theta)$ solves the Elrod–Adams model (3).*

Proof. Let $\theta = T(\theta)$ be a fixed point of the operator T and $p = \mathcal{P}(\theta)$ the corresponding pressure. Without loss of generality, we assume that the domain Ω is defined as $\Omega = [0, 1]$ and that the cavitation domain $\Omega_0(p)$ is given by the interval $[x_0, x_1]$ with $0 < x_0 \leq x_1 < 1$. In the case of multiple cavitation domains, the following argumentation can be carried out on each domain separately. Due to the definition of $\Omega_0(p)$, the following conditions hold on the cavitation boundary

$$p(x_0) = 0, \quad p(x_1) = 0, \quad p'(x_0^+) \leq 0, \quad p'(x_1^-) \geq 0. \tag{30}$$

As a first step, we show that the pressure fulfills $p = 0$ in $\Omega_0(p)$ by a monotonicity argument. For this purpose, we utilize $p = \mathcal{P}(\theta)$ and integrate the corresponding PDE (3a) from x_0 to $x \in [x_0, x_1]$

$$\int_{x_0}^{x} -\left(h^3 p'\right)' \,\mathrm{d}x = \int_{x_0}^{x} -(\theta h)' \,\mathrm{d}x. \tag{31}$$

Since θ is Lipschitz continuous on $\Omega_0(p)$, we can use the fundamental theorem of calculus to obtain

$$h(x_0)^3 p'(x_0) - h(x)^3 p'(x) = \theta(x_0)h(x_0) - \theta(x)h(x). \tag{32}$$

Inserting $\theta = \min\{C(p), 1\}$ together with the analytical representation (8) into the equation yields an expression for the pressure derivative at the point x

$$p'(x) = h(x)^{-3} \left(\min\left\{ \frac{h(x_0)}{h(x)}, 1 \right\} h(x) - h(x_0) + h(x_0)^3 p'(x_0^+) \right). \tag{33}$$

Since $h(x) > 0$ and $p'(x_0) \leq 0$, we get $p'(x) \leq 0$ for all $x \in [x_0, x_1]$. This means that p is monotonically decreasing in $\Omega_0(p)$. Using $p(x_0) = 0$ and $p(x_1) = 0$ we conclude that $p = 0$ in $\Omega_0(p)$.

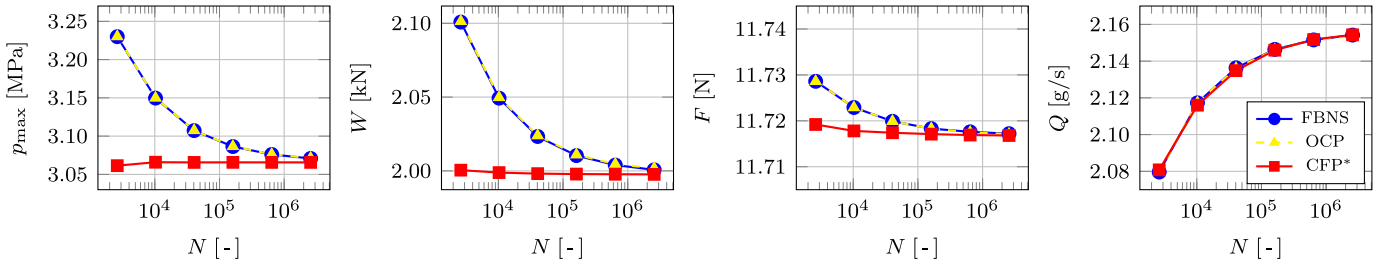

Fig. 9. Convergence of the performance parameters $p_{\max}$, W, F and Q of the eccentric journal bearing. The OCP and FBNS algorithms use $\mathcal{P}_\Delta(\theta)$ while the CFP* algorithm uses $\mathcal{P}^*_\Delta(\theta)$.

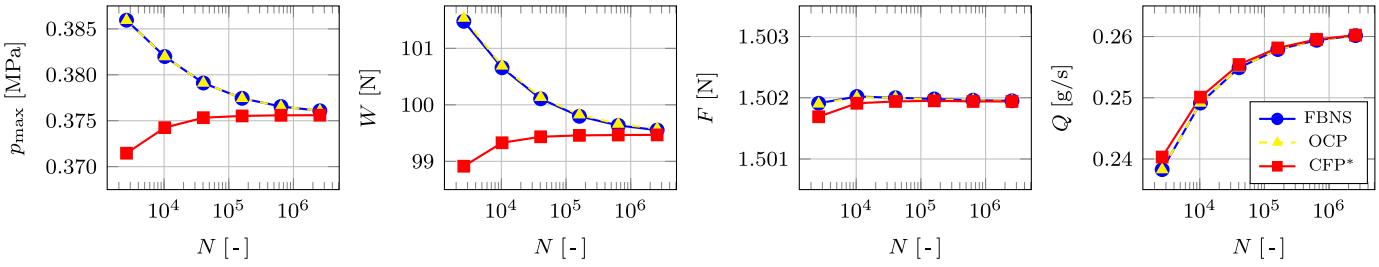

Fig. 10. Convergence of the performance parameters $p_{\max}$, W, F and Q of the misaligned journal bearing. The OCP and FBNS algorithms use $\mathcal{P}_\Delta(\theta)$ while the CFP* algorithm uses $\mathcal{P}^*_\Delta(\theta)$.

Next we show that (p,θ) fulfills the Elrod–Adams system (3). As a direct consequence of $p = 0$ in $\Omega_0(p)$ we obtain $p \geq 0$ in Ω. Since $\theta = \min\{C(p), 1\}$, we know that $0 \leq \theta \leq 1$ in Ω and $\theta = 1$ in $\Omega \setminus \Omega_0(p)$. Combined with $p = 0$ in $\Omega_0(p)$ this yields $(1-\theta)p = 0$. Collecting all results we get $p \geq 0$, $0 \leq \theta \leq 1$, $(1-\theta)p = 0$ and $p = \mathcal{P}(\theta)$, which means that $(\mathcal{P}(\theta), \theta)$ solves the Elrod–Adams model (3). □

Appendix B

Here we derive the linear system of equations in $\mathcal{P}_\Delta(\theta)$ that arises from the FEM in Section 6. For this purpose, we need to use the weak formulation of (3a). By multiplying a test function $\phi \in C_0^\infty(\Omega)$ to the equation and integrating over Ω we obtain

$$\int_\Omega -\nabla\cdot\left(h^3\nabla p\right)\phi\,\mathrm{d}\boldsymbol{x} = \int_\Omega -\nabla\cdot(\theta h\boldsymbol{e})\,\phi\,\mathrm{d}\boldsymbol{x}. \tag{34}$$

Integrating by parts with vanishing boundary terms on both sides yields the weak formulation

$$\int_\Omega h^3\nabla p\cdot\nabla\phi\,\mathrm{d}\boldsymbol{x} = \int_\Omega \theta h\boldsymbol{e}\cdot\nabla\phi\,\mathrm{d}\boldsymbol{x}. \tag{35}$$

We denote the grid used in Section 6 as $\mathcal{T}(\Omega)$ and cells of the grid as $E \in \mathcal{T}(\Omega)$. Due to the periodic boundary conditions, the nodes of the grid on the right boundary are identified with the corresponding nodes on the left boundary. The DoFs are then given by the remaining nodes which we denote as $\mathcal{N} = \{1,\dots,N\}$. Each DoF $j \in \mathcal{N}$ is associated with a shape function ϕ_j that is piecewise bilinear on $\mathcal{T}(\Omega)$, evaluates to 1 at the jth node, and vanishes at every other node. Using these functions, we can approximate the pressure p and liquid ratio θ by

$$p \approx \sum_{j\in\mathcal{N}} p_j\phi_j, \quad \theta \approx \sum_{j\in\mathcal{N}} \theta_j\phi_j, \tag{36}$$

with coefficient vectors $\boldsymbol{p},\boldsymbol{\theta} \in \mathbb{R}^N$. In order to deal with the Dirichlet boundary condition, we divide the DoFs $\mathcal{N}$ into DoFs located on the upper/lower boundary or in the supply zone $\mathcal{B} \subset \mathcal{N}$ and the remaining inner DoFs $\mathcal{I} = \mathcal{N}\setminus\mathcal{B}$. Inserting the approximations (36) into the weak formulation (35) and testing the equation with ϕ_i for $i \in \mathcal{I}$ results in

$$\sum_{j\in\mathcal{N}} p_j \int_\Omega h^3\nabla\phi_j\cdot\nabla\phi_i\,\mathrm{d}\boldsymbol{x} = \sum_{j\in\mathcal{N}} \theta_j \int_\Omega \phi_j h\boldsymbol{e}\cdot\nabla\phi_i\,\mathrm{d}\boldsymbol{x}. \tag{37}$$

By setting the boundary coefficients $\{p_j\}_{j\in\mathcal{B}}$ to the Dirichlet value p_d, which corresponds to the ambient pressure p_a or the supply pressure p_s, and transforming we obtain

$$\sum_{j\in\mathcal{I}} p_j \int_\Omega h^3\nabla\phi_j\cdot\nabla\phi_i\,\mathrm{d}\boldsymbol{x} = \sum_{j\in\mathcal{N}} \theta_j \int_\Omega \phi_j h\boldsymbol{e}\cdot\nabla\phi_i\,\mathrm{d}\boldsymbol{x} - \sum_{j\in\mathcal{B}} p_d \int_\Omega h^3\nabla\phi_j\cdot\nabla\phi_i\,\mathrm{d}\boldsymbol{x}. \tag{38}$$

Since this equation needs to hold for every ϕ_i, $i \in \mathcal{I}$, we obtain $\#\mathcal{I}$ linear equations for the inner coefficients $\{p_j\}_{j\in\mathcal{I}}$. By adding $\#\mathcal{B}$ equations for the constrained boundary coefficients $\{p_j\}_{j\in\mathcal{B}}$, we obtain the linear system of equations

$$\mathbf{A}\boldsymbol{p} = \mathbf{B}\boldsymbol{\theta} + \boldsymbol{c}, \tag{39}$$

where the matrices $\mathbf{A},\mathbf{B} \in \mathbb{R}^{N\times N}$ and the vector $\boldsymbol{c} \in \mathbb{R}^N$ are given by

$$\mathrm{A}_{ij} = \begin{cases} 1 & \text{if } i = j \in \mathcal{B}, \\ \int_\Omega h^3\nabla\phi_j\cdot\nabla\phi_i\,\mathrm{d}\boldsymbol{x} & \text{if } i,j \in \mathcal{I}, \\ 0 & \text{else,} \end{cases} \tag{40}$$

$$\mathrm{B}_{ij} = \int_\Omega \phi_j h\boldsymbol{e}\cdot\nabla\phi_i\,\mathrm{d}\boldsymbol{x}, \tag{41}$$

$$c_i = \begin{cases} p_d & \text{if } i \in \mathcal{B}, \\ -\sum_{j\in\mathcal{B}} p_d \int_\Omega h^3\nabla\phi_j\cdot\nabla\phi_i\,\mathrm{d}\boldsymbol{x} & \text{else.} \end{cases} \tag{42}$$

The integrals are approximated by a quadrature rule on each cell. Given a set of quadrature points $x_1,\dots,x_M \in [0,1]^2$ with corresponding weights $w_1,\dots,w_M \in \mathbb{R}$, the integral over a cell E can be approximated by

$$\int_E f(x)\,\mathrm{d}\boldsymbol{x} \approx \sum_{q=0}^{M} f(x_q)w_q|\det(J_E)|, \tag{43}$$

where J_E describes the Jacobian of the coordinate transformation from E to the reference cell $[0,1]^2$. A common choice for the quadrature rule is the Gauß-Lobatto quadrature, which we use for $\mathbf{A}$ and $\boldsymbol{c}$ as well as for $\mathbf{B}$ in the non-stabilized case. In order to stabilize the system for the OCP and FBNS algorithm, we use an upwind quadrature for $\mathbf{B}$ given by a single quadrature point $x_q = (0,0)$ with weight $w_q = 1$.

Data availability

Data will be made available on request.

References

[1] Reynolds O. On the theory of lubrication and its application to Mr. Beauchamp Tower's experiments, including an experimental determination of the viscosity of olive oil. Philos Trans R Soc 1886;177:157–234.

[2] Gümbel L. Vergleich der Ergebnisse der rechnerischen Behandlung des Lagerschmierungsproblems mit neueren Versuchsergebnissen. In: Mbl. Berl. Bez. VDI. 1921.

[3] Swift HW. The stability of lubricating films in journal bearings. In: Minutes of the proceedings of the institution of civil engineers 233. 1932, p. 267–88.

[4] Stieber W. Das Schwimmlager: Hydrodynamische Theorie des Gleitlagers. VDI-Verlag; 1933.

[5] Ausas RF, Ragot P, Leiva J, Jai M, Bayada G, Buscaglia GC. The impact of the cavitation model in the analysis of microtextured lubricated journal bearings. J Tribol 2007;129(4):868–75.

[6] Jakobsson B, Floberg L. The finite journal bearing, considering vaporization. Gothenburg: Trans. Chalmers Univ. of Tech; 1957, p. 190.

[7] Olsson K. Cavitation in dynamically loaded bearings. Gothenburg: Trans. Chalmers Univ. of Tech; 1965, p. 308.

[8] Elrod HG, Adams ML. A computer program for cavitation and starvation problems. In: Proceedings of the first LEEDS-LYON symposium on cavitation and related phenomena in lubrication. 1975, p. 37–41.

[9] Elrod HG. A cavitation algorithm. J Lubr Technol 1981;103(3):350–4.

[10] Bayada G, Martin S, Vázquez C. Two-scale homogenization of a hydrodynamic Elrod-Adams model. Asymptot Anal 2005;44:75–110.

[11] Bayada G, Chupin L. Compressible fluid model for hydrodynamic lubrication cavitation. J Tribol 2013;135(4):041702.

[12] Ransegnola T, Sadeghi F, Vacca A. An efficient cavitation model for compressible fluid film bearings. Tribol Trans 2021;64(3):434–53.

[13] Bayada G, Chambat M, Vázquez C. Characteristics method for the formulation and computation of a free boundary cavitation problem. J Comput Appl Math 1998;98(2):191–212.

[14] Ausas RF, Jai M, Buscaglia GC. A mass-conserving algorithm for dynamical lubrication problems with cavitation. J Tribol 2009;131(3):031702.

[15] Profito FJ, Giacopini M, Zachariadis DC, Dini D. A general finite volume method for the solution of the Reynolds lubrication equation with a mass-conserving cavitation model. Tribol Lett 2015;60(18):1573–2711.

[16] Tber MH. An active-set mixed finite element solver for a transient hydrodynamic lubrication problem in the presence of cavitation. ZAMM - J Appl Math Mech / Z Für Angew Math Und Mech 2017;98:999–1014.

[17] Giacopini M, Fowell MT, Dini D, Strozzi A. A mass-conserving complementarity formulation to study lubricant films in the presence of cavitation. J Tribol 2010;132(4):041702.

[18] Woloszynski T, Podsiadlo P, Stachowiak GW. Efficient solution to the cavitation problem in hydrodynamic lubrication. Tribol Lett 2015;58:1573–2711.

[19] Rom M. Physics-informed neural networks for the Reynolds equation with cavitation modeling. Tribol Int 2023;179:108141.

[20] Cheng Y, He Q, Huang W, Liu Y, Li Y, Li D. Hl-nets: Physics-informed neural networks for hydrodynamic lubrication with cavitation. Tribol Int 2023;188:108871.

[21] Brumand-Poor F, Barlog F, Plückhahn N, Thebelt M, Bauer N, Schmitz K. Physics-informed neural networks for the Reynolds equation with transient cavitation modeling. Lubricants 2024;12.

[22] Marian M, Almqvist A, Rosenkranz A, Fillon M. Numerical micro-texture optimization for lubricated contacts—a critical discussion. Friction 2022;10:1772–809.

[23] Xu W, Wang X, Huang T, Yang J. Efficient implementation of numerical methods for solving bearing cavitation problems using symmetric system solvers. Tribol Int 2023;186:108624.

[24] Dong Q, Cho YJ, He S, Pardalos PM, Rassias TM. The Krasnoselskii-Mann iterative method. Springer Cham; 2022.

[25] Byrd RH, Lu P, Nocedal J, Zhu C. A limited memory algorithm for bound constrained optimization. SIAM J Sci Comput 1995;16(5):1190–208.

[26] LeVeque RJ. Finite volume methods for hyperbolic problems. Cambridge University Press; 2002.

[27] Tröltzsch F. In: Optimal control of partial differential equations, vol. 112, American Mathematical Society; 2010.

[28] Liu DC, Nocedal J. On the limited memory BFGS method for large scale optimization. Math Program 1989;45:503–28.

[29] Bertocchi L, Dini D, Giacopini M, Fowell MT, Baldini A. Fluid film lubrication in the presence of cavitation: a mass-conserving two-dimensional formulation for compressible, piezoviscous and non-Newtonian fluids. Tribol Int 2013;67:61–71.

[30] Bangerth W, Hartmann R, Kanschat G. deal.II - A general-purpose object-oriented finite element library. ACM Trans Math Softw 2007;33(4). 24/1–271.

[31] Toewe D, Qiu Y. LBFGS++. 2023, https://lbfgspp.statr.me/. [Online; Accessed 10 December 2024].

[32] Davis TA. Algorithm 832: UMFPACK V4.3 - an unsymmetric-pattern multifrontal method. ACM Trans Math Software 2004;30(2):196–9.

[33] Maulén JJ, Fierro I, Peypouquet J. Inertial Krasnoselskii-Mann iterations. Set-Valued Var Anal 2024;32(2):10.